Universitat Autònoma de Barcelona

Escola d'enginyeria

Growth and characterization of CoO ultra thin films

Final project submitted by

Manel Molina Ruiz

to apply for the degree of Materials Engineering

Director Dr. Aitor Lopeandía Fernández

Grup de Nanomaterials i Microsistemes

Departament de Física

Bellaterra, September 2011

El Dr. Aitor Lopeandía Fernández, professor lector del Departament de Física de la Facultat de Ciències de la Universitat Autònoma de Barcelona.

CERTIFICA: que en Manel Molina Ruiz, ha realitzat sota la seva direcció el treball que porta com a títol *"Growth and characterization of CoO ultra thin films"*, el qual es recull en aquesta memòria per tal d'optar al Títol d'Enginyer de Materials per la Universitat Autònoma de Barcelona.

Dr. Aitor Lopeandía Fernández

Bellaterra, Setembre 2011

Agraïments

Voldria agrair a totes les persones que m'han ajudat, tant en la realització d'aquest Projecte Final de Carrera per optar al títol d'Enginyer de Materials, així com les que m'han ensenyat i de les que he aprés.

En especial als companys del Grup de Nanomaterials i Microsistemes (GNaM) de la Universitat Autònoma de Barcelona, amb els que he conviscut i dels que he aprés tot el relacionat amb aquest món. A vosaltres Gemma, Marta, Iris, Cristian, Pablo i Jordi. A en Javier Rodríguez Viejo, perquè em vas donar la opció de continuar els estudis d'enginyeria i he arribat a la seva consecució. En particular necessito donar les gràcies al Dr. Aitor Lopeandía Fernández per la teva dedicació i interès, per la paciència que has hagut de tenir i el seguiment que m'has ofert, per acceptar ser el meu director i per moltes altres coses que no tinc temps a dir.

Un agraïment especial mereix el Dr. Francesc Pi, per deixar-nos fer servir i realitzar canvis en la configuració de la cambra d'evaporació. Per ser mestre i company.

Voldria agrair també al Dr. Olivier Boureois de l'Institut Néel del CNRS a Grenoble per les profitoses discussions sobre magnetisme i nanocalorimetria.

Al Dr. Francesc Xavier Muñoz i al seu equip d'investigació de l'Institut de Microelectrònica de Barcelona (IMB-CNM) per la col·laboració en els processos

tecnològics de microfabricació dels dispositius per poder realitzar les mesures de nanocalorimetria.

I finalment, als tècnics del Servei de Microscòpia Electrònica (SME) i de Difracció de Raigs X de la Universitat Autònoma de Barcelona per l'ajuda que he rebut en la preparació de les mostres i posterior anàlisi.

Per altra banda vull agrair el suport rebut durant tot el temps que he hagut de dedicar a aquest projecte, en especial a dues persones. A l'Aïda, per tots els moments que hem passat des de que varem començar la carrera. I a l'Ana, per la paciència que has tingut amb mi, per les hores que m'has concedit perquè ho pogués dur a bon terme.

A tots vosaltres i per molt diverses raons,

gràcies !

Contents

List of Figures

List of Tables

Chapter 1

Motivation of this work

During last years, the cobalt oxide (CoO) has been widely studied for its magnetic properties [1, 2, 3, 4]. This material shows an antiferromagnetic (AF) behavior below a critical temperature, called Néel temperature (T_N), and becomes paramagnetic (PM) above it. This property promotes very interesting applications when the AF material is combined with a ferromagnetic (FM) one, such as giant magnetoresistance (GMR) [5, 6] or exchange bias (EB) [7, 8] with applications as spin valves or magnetic recording media heads respectively. Most of these applications need to use the material in thin film form and the magnetic properties may be strongly dependent on its microstructure. Moreover with the size reduction of the material to the nanoscale range its physical properties may also be affected.

In this project we target, as an objective, *(i)* the growth of the correct phase of CoO, in ultra thin films form, onto amorphous substrates using reactive electron beam physical vapor deposition, *(ii)* the structural and morphological characterization of the samples with the thickness and *(iii)* the magnetic characterization using *in-situ* nanocalorimetry.

In a short future, this information will be used to study by nanocalorimetry the Néel wall formation on CoO/Co exchange biased coupled layers. For that,

nanocalorimetry is the unique technique that permits to access the magnetic information in single antiferromagnetic ultra thin films. Even for bulk antiferromagnetic materials, the magnetic signature obtained by magnetometric techniques is very weak. When the samples are in the nanoscale range, the large ratio of surface atoms promotes loosely coupled spins that typically dominate the magnetic signature shadowing the antiferromagnetic component. Unlike magnetometric measurements, heat capacity is a fundamental magnitude that reports information about all the entropy changes in the sample volume, which is especially necessary to measure antiferromagnets. Nevertheless, nanocalorimetry does not report any information about the morphology or microstructure of the sample, thus X-ray diffraction and transmission electron microscopy with electron diffraction and electron dispersive X-ray diffraction are used as complementary techniques.

In general, we are interested on how magnetic properties of magnetic oxides change when the sample size reaches the nanoscale.

Chapter 2

Introduction

The history of magnetism and magnetic materials began thousands of years ago in the ancient Chinese civilization, where first mentions of magnetic phenomena in iron oxides based minerals (lodestones) were reported by Guanzhong (died 645 B.C.). Magnetic attraction was the first phenomenon to draw the attention of man to lodestone. In Greece Aristotle reported that Thales of Miletus (625 B.C.) also knew about lodestones and its magical properties. However, it was Onomacritus who baptize for the first time one of the most famous magnetic minerals the Fe_3O_4 as *magnetes*. The name arises because its abundance in the Greek prefecture of Magnesia. This is the most ancient name known which evolved into the modern term magnetite and also the name for the physical phenomena, *magnetism*. During centuries the main technological application was the compass, and no serious theories were performed, as noted Denis Diderot and Jean Lerond d'Alembert in their Encyclopaedia. At that time the knowledge of magnetism was summarized under three entries: magnetic poles, attraction, and transmission of magnetism. The Encyclopaedists had to face the fact that all attempts at interpreting magnetism (including the efforts of the mathematician Bernoulli) were unsuccessful. We would need to wait until the 19th century to observe a clear advances

on the theories about magnetism, due to a series of great contributions: Charles de Coulomb demonstrated his famous $1/r^2$ interaction law between "magnetic charges", Denis Poisson introducing the notion of a magnetic field, H. C. Oersted showing that a magnetic field could be created by the circulation of an electric current in a conducting wire André-Marie Ampére repeated this historic experiment, and succeeded in giving it an elegant formulation, Michael Faraday discovered the phenomenon of induction and developed the first dynamo and James Clerk Maxwell in 1864 crowned the efforts of half a century with the laws of the electromagnetism, which remain today in the analytical basis of magnetism. It was close to the beginning of the 20th century were we could find the first serious works on describing the magnetism in magnetic materials. From the classical point of view, the work of Pierre Curie clarified some ideas on diamagnetism, paramagnetism and ferromagnetism [9], Paul Langevin established the statistical theory of paramagnetism [10] and Pierre Weiss the molecular field theory [11]. The necessity for giant molecular field to explain the magnetism in several substances evidenced the limitations of the theory. At this stage, in 1927, the quantum mechanics made a fundamental contribution to magnetism with the discovery by Paul Dirac of the intrinsic angular momentum of the electron, called spin [12]. Afterthat, in 1929, Werner Heisenberg showed the electrostactic origin of the magnetic interactions responsible of the magnetic order, and how it could be interpreted in terms of coupling between two neighbouring spins [13]. With the exchange theory the huge magnetic field created in most ferromagnetic materials was perfectly explained.

It was in 1936, when Louis Néel established the model for a new kind of magnetism, the antiferromagnetism [14]. Several years later, in 1948 he published the paper entitled *"Les proprieties magnétiques des ferrites: ferrimagnétisme et antiferromagnétisme"* [15], where he generalized his theory of antiferromagnetic materials supposing that the two magnetic sublattices which compose it have un-

equal magnetic moments ($\overrightarrow{m}$). His theory predicted a novel behavior, the ferrimagnetism, where the spins are aligned antiparallel in a system composed by two lattices with different magnetic moment every one, which produces a nonzero magnetization. In fact, antiferromagnetism is a particular case of ferrimagnetism where both lattices have the same magnetic moment. During last 50 years, a large number of engineering applications using antiferromagnets have been developed.

2.1 The physics of magnetism

The magnetism in matter may be originated by the orbital motion of electrons rotating around the nuclei or by its intrinsic spin. The orbital magnetic moment of the electron is proportional to its orbital angular momentum. In an atom, for each electron with an angular quantum number $+l$ uses to be another with $-l$ cancelling its action. Thus the net result is that, for most materials, the magnetic effect produced by the orbital motion of the electrons is either zero or very small. Very different is the case of the spin contribution. Considering the Pauli Exclusion Principle (i.e. the electron behaves as fermions) and the Hund's Rules for filling the electronic orbitals in an atom, it is find for a given atomic number (Z) that unbalanced spins will result on a net magnetic moment. This is the case for iron, cobalt and nickel, the only three elements showing ferromagnetic behaviour (except some rare earths). In the Figure 2.1, a schematics of the electronic structure of cobalt [Ar].4s2.3d7 is showed, where 3 electrons of the *d* orbital interact giving a nonzero magnetic moment.

Substances can be classified depending on the magnetic nature of the atoms (if they show a permanent magnetic moment or not) and how this magnetic moment interact between them. One big family is formed by the substances made of atoms that do not present a permanent magnetic moment, the Diamagnetic substances.

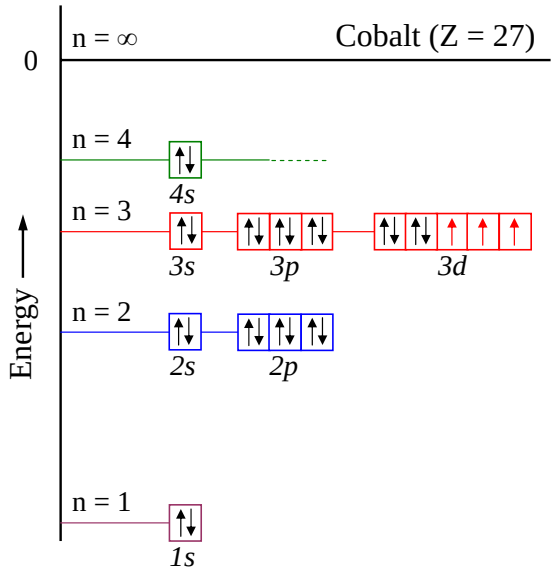

Figure 2.1: Schematics of the electronic structure of cobalt.

In the presence of an external magnetic field, those substances react creating a very weak and permanent magnetization in the opposite direction. Of course, the other big family includes all the substances with permanent magnetic moment in the atoms or in the molecules that form them. Among them we can identify as Paramagnetic substances those there is no interaction between the magnetic moment, and without applied magnetic field, present null magnetization due to the disorder introduced by the thermal fluctuation. When an external magnetic field is applied, it interacts with the magnetic moments beating the thermal disorder aligning some of them in the field direction and promoting a weak positive magnetization. Finally, there is a small number of substances where the atoms (or molecules) have permanent magnetic moments that interact between them. This interaction is defined the coupling between neighboring spins. As Heisenberg, defined the exchange integral (J) defined in Equation 2.1, where J is the sum over all pairs i, j, of an interaction term.

$$J(i,j) = \iint \psi_i^*(r_1)\psi_j^*(r_2)\frac{1}{r_{12}}\psi_i(r_2)\psi_j(r_1)\, dr_1 dr_2 \tag{2.1}$$

Experimetally, the value of the exchange integral J depends strongly on the cristalline structure (distance between atoms) and the electrostactic interaction between the orbitals. Bethe and Slater, found the empirical curve where the value of *J* where plotted as a function of the ratio between the atomic and the 3d shell radiuses for different elements on the periodic table (Figure 2.2).

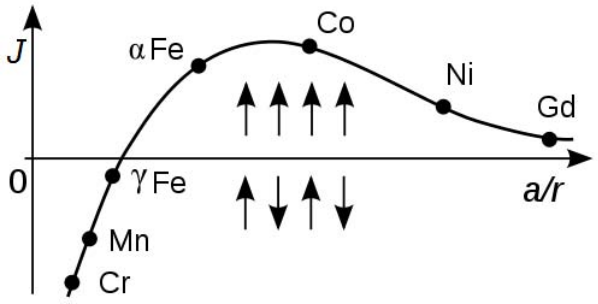

Figure 2.2: Bethe-Slater curve where the x-axis gives the ratio of radius of atom (a) to the radius of 3d shell of electron (r). The elements with positve exchange integral term (*J*) shows ferromagnetic nature such as Fe, Co and Ni and elements with negative *J* shows antiferromagnetic nature.

When $J > 0$ indicates a ferromagnetic interaction and the magnetic moments of the atoms or molecules are aligned in regular patterns with neighboring spins pointing on the same direction. On the other hand, when $J < 0$ the exchange interation tend to anti-align neighboring spins. In antiferromagnetic materials, the magnetic moments of atoms or molecules, are aligned in a regular pattern with neighboring spins (on different sublattices) pointing in opposite directions. When no external field is applied, the antiferromagnetic structure corresponds to a vanishing net magnetization. As shows Figure 2.3 antiferromagnetism is a particular

case of ferrimagentism where the magnetic moments of the two sublattices are unequal, and thus the cancelation of the magnetization is not completed.

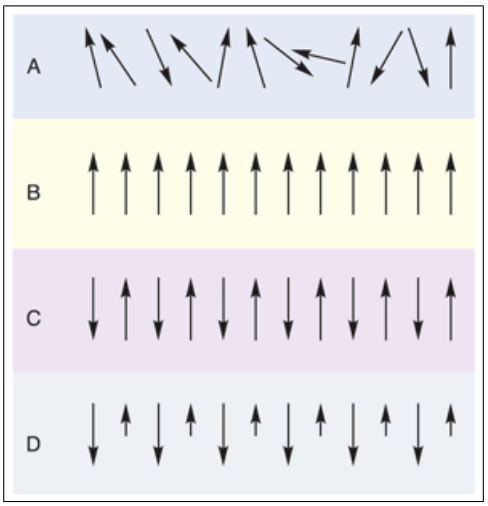

Figure 2.3: Types of magnetism: (A) paramagnetism, (B) ferromagnetism, (C) antiferromagnetism and (D) ferrimagnetism.

When a field is applied, a kind of ferrimagnetic behavior may be displayed in the antiferromagnetic phase. Due to the field interaction promoting the alignment with the field in one sublattice and thermal agitation disordering the other, the absolute value of magnetization on one sublattice differs from that of the another, resulting in a nonzero net magnetization. The maximum on the net magnetization in the antiferromagnet is achieved for a critical temperature where the order-disorder transition occurs, known as Néel point, and the highest the Néel temperature the highest the antiferromagnetic exchange coupling energy.

Tipically, magnetic materials are characterized by its susceptibility (χ). It is a magnitude that relates the magnetization on the sample in the presence of a given applied magnetic field. Nevertheless, susceptibility experimental measurements of antiferromagnets are very complicated due to the weakness of the signature

even for bulk samples. The reason is that the total magnetization on these materials is null or very small ($\overrightarrow{M} \simeq 0$), then magnetometric techniques are not enough sensitive. The heat capacity is sensitive to any change on the energy within the sample volume, i.e. their atoms, and the interaction between the spins is related with the magnetic entropy, which one changes when a magnetic transition occurs. Then the heat capacity reveals information about the own magnetic transition.

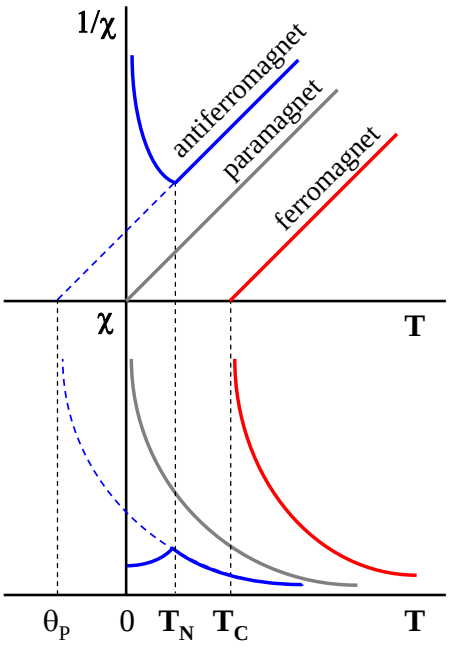

Figure 2.4: Magnetic susceptibility and the inverse of magnetic susceptibility versus temperature for paramagnetic, ferromagnetic and antiferromagnetic materials.

The Figure 2.4 shows the magnetic susceptibility for different magnetic materials. An antiferromagnetic material typically shows a maximum at the Néel temperature, where the material passes from antiferromagnet to paramagnet. In contrast, at the transition between the ferromagnetic to the paramagnetic states the susceptibility will diverge.

2.2 The cobalt oxide system

The CoO system has two stable phases, the cobalt oxide (II) or monoxide (CoO) and the cobalt oxide (III) (Co_3O_4). The first one is stable up to 1000 ^oC when in presence of oxygen turns to Co_3O_4. The obtention of one or another from pure metallic cobalt depends on the temperature and partial pressure of oxygen. Moreover, CoO has two metastable structures known as zinc blende (ZB) and wurtzite types which are not desirables when magnetic properties are studied. The reason of a magnetic behaviour demonstration or not in the CoO periclase[1] (salt rock - SR) structure is a structural contraction along the cubic [100] directions between the paramagnetic state which corresponds to a cubic structure, the salt rock type (space group $Fm\bar{3}m$) and the AF state coupled to a tetragonal structure (space group I4/mmm) [16, 17, 18]. Over the years, different works established this transition in a range between 288 K and 293 K for the bulk [19, 20].

The election of CoO is due to its large magnetic moment and to the value of its magnetic transition temperature. Its magnetic moment promotes a bigger heat capacity signal, and the value of its T_N allows engineering applications because of it is located around room temperature, when compared with other stable magnetic salt rock monoxides (NiO and MnO respectively) [21, 22]. The FeO is not considered because this phase is unstable below 575 ^oC and decomposes following the reaction: $4FeO \rightarrow Fe + Fe_3O_4$ [23].

The Figure 2.5 represents the CoO, with the rock salt crystal structure that shows the PM state (in this structure the magnetic alignment is clearly evidenced unlike the tetragonal one. For this reason this structure will be used for further explanations). The spins on some nearest-neighbour transition metal ions are parallel, (a) and (b); those on other nearest neighbours are antiparallel, (b) and (c).

[1] Periclase occurs naturally in contact metamorphic rocks.

But next nearest neighbours always have antiparallel spins: (a) and (c) or (c) and (d). Thus the spins within a given (111) plane are parallel to each other and antiparallel to those on the two adjacent (111) planes.

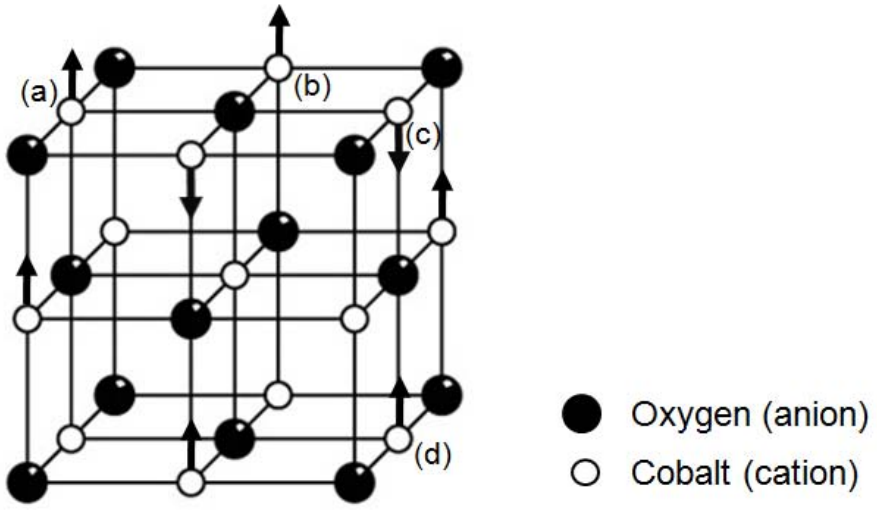

Figure 2.5: Rocksalt structure common to transition metal monoxides. The spin structure of CoO is indicated by arrows on the transition metal ions.

The physical explanation for the magnetic interaction in this kind of oxides can not be found in a simple Heisenberg exchange interaction between first neighbourgs ($H = -2J \sum \mathbf{S}_i \cdot \mathbf{S}_j$). The strength of the exchange interaction depends on orbital overlap. The Heisenberg form of exchange applies to some localized systems, but fails even for oxide magnets such as CoO. The magnetic behaviour of transition metal oxides is governed by a less familiar form of exchange. In that systems, there must be a magnetic interaction that couples second nearest neighbours so that their spins have opposite orientations. That way, oxygen atoms always lie midway on the line between next nearest neighbours. Next-nearest neighbour sites, two lattice constants apart, are too far apart to be involved in Heisenberg exchange, there is just not enough wavefunction overlap. Therefore

some form of mediated or "indirect" exchange interaction must be operating, the superexchange. This model proposed by Louis Néel and formulated in detail by Anderson [24], describes this effect quite well. Superexchange operates in many ionic oxides and coupled localized, usually *3d*, moments.

2.3 The nanomagnetism in oxides

Nanomaterials like the CoO layers explored here, in general, if there are structural irregularities, present a large ratio of atoms placed on the surfaces, grain boundaries or defects that are imperfect from the crystalline point of view. The superexchange, as it also happened with the Heissenberg exchange is highly dependent on the crystalline structure.

At the nanoscale, due to the superficial stress, there is a crystallinity decrease, which modifies the distances between atoms and then the J is changed also. Remembering the Bethe Slater curve (Figure 2.2) and the Equation 2.1, if the exchange integral changes a particular material may exhibit magnetic behaviour or not. The geometrical frustration [25] or the competing FM and AF interactions may lead to different and, perhaps, more complicated magnetic structures like magnetic dead layers or spin glasses, loosely coupled spins/ldots The magnetic dead layers act as a wall, limiting the magnetic interaction through them. The loosely coupled spins are spins of atoms which do not interact with the others, but in the presence of an external field they act as a paramagnet.

All these phenomena may disguise the real nature and properties of magnetic nanomaterials and is of crucial importance a deep knowledge of them, booth structural and magnetic.

Chapter 3

Experimental procedure

In this chapter we detail the procedure of followed to obtain the CoO thin film samples, form the bulk like to the 1nm thick, and the different characterization techniques used.

3.1 Preparation of the samples

3.1.1 Substrates selection and preparation

In this study, all the samples have been deposited over the same base material: the amorphous silicon nitride (SiN_X). As all the substrates used to characterize the samples have this material we to avoid structural variations between samples due to chemical interaction at the surface of the substrate. So that, commercial silicon nitride coated Si wafer (100) have been diced onto pieces of around 1×1 cm^2. These pieces have been used for the bulk characterization and two different substrates for the nanoscale characterization: silicon nitride membrane window (20 nm thickness, 0.5×0.5 mm^2 area) from SPI Supplies and membrane based devices nanocalorimeters [26] (180 nm thickness and 1.085 mm^2 of effective sensing area) microfabricated in collaboration with the Institut de Microelectrònica de

Barcelona (IMB-CNM).

3.1.2 Electron beam physical vapour deposition

All the CoO samples have been prepared at the Laboratory of thin films of the Sciences Faculty at the Universitat Autònoma de Barcelona in collaboration with the Professor Francesc Pi. The setup consists on an electron beam physical vapour deposition (EB-PVD) evaporator mounted inside a Leybold UNIVEX 450 high vacuum (HV) chamber (Figure 3.1).

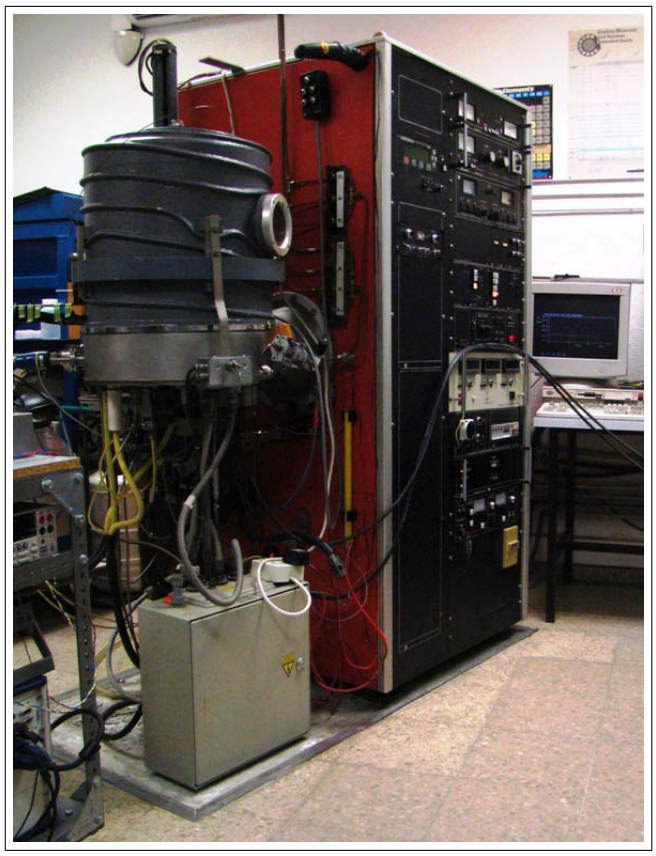

Figure 3.1: Leybold UNIVEX 450 vacuum chamber with e-Gun ESV 4 electron beam installed inside.

The EB-PVD is a form of physical vapor deposition in which a target anode is

bombarded with an electron beam given off by a charged tungsten filament under high vacuum. The electron beam transforms into the gaseous phase the atoms from the target. These atoms then precipitate into solid form, coating everything in the vacuum chamber (within line of sight) with a thin layer of the anode material.

This technique is interesting for this project because the deposition rate can be as low as 1 nm per minute to as high as few micrometers per minute. The material utilization efficiency is high relative to other methods and the process offers structural and morphological control of films. Due to the very high deposition rate compared with other PVD deposition techniques, this process has potential industrial applications. The only one disadvantage for EB-PVD is the directionality of deposition process. The translational and rotational motion of the shaft helps for coating the outer surface of complex geometries, but this process cannot be used to coat the inner surface of complex geometries. Another potential problem is that filament degradation in the electron gun results in a non-uniform evaporation rate [28]. For this reason our study and possible applications will be limited to a planar geometry.

Deposition parameters have been optimized to grow polycrystalline CoO thin films onto amorphous SiN_X substrates by reactive PVD. Cobalt atoms have been evaporated from a cobalt metallic target (99.95 % purity pellets) by EB-PVD into oxygen rich atmosphere to promote the in-flight oxidation before it reaches the substrate. An initial set of samples varying the substrate temperatures, deposition rates and oxygen partial pressures (P_{O_2}) have been performed to check the influence of each parameter on the final samples. On this initial set all the samples have been grown with thicknesses around 60 nm to allow their characterization by means of X-ray diffraction. The thicknesses has been measured by means of a crystal quartz monitor using as density value 6.44 g/cm^3 [27], the corresponding for the bulk CoO. Once the parameters were optimized, a second set of thinner

samples with thickenesses ranging from 1 to 20 nm were grown.

3.2 Characterization of the samples

As mentioned previously, different types of substrates have been selected apriori, considering the compatibility substrate/technique, to enable the structural and morphological characterization of CoO the samples grown on top. The criteria used on the selection of the techniques have been the information that they could report to us. The initial objective was to achieve the deposition conditions to obtain the correct CoO phase in bulk samples, or thick films. So that, different conditions have been tested and the resulting layers have been characterized by regular X-ray diffraction (XRD). As it is well known, in the initial stages of growth, when the evaporated specimen condensates directly onto the substrate, the local microstructure of the sample could change from the one we find on top of the thick (bulk) samples. Moreover, it is well know that for nanoscale samples metastable phases could be potentiated by surface effects. In order to check if with the optimal conditions found for bulk samples, the thinner samples maintain the same phase and structure, complementary characterization techniques have been used: transmission electron microscopy (TEM), electron diffraction (ED) and energy dispersive X-ray spectroscopy (EDS). To characterize the magnetic transition, we have used the quasiadiabatic nanocalorimetry that, as we mention previously, results a unique technique when analyzing the thermodynamic magnetic transition on antiferromagnets with thicknesses below 10 nm.

3.2.1 Bulk characterization

X-ray scattering techniques are a family of non-destructive analytical techniques which reveal information about the crystallographic structure, chemical compo-

sition and physical properties of materials and thin films. These techniques are based on observing the scattered photon intensity of an X-ray beam hitting a sample as a function of incident and scattered angle, polarization and wavelength or energy. The XRD yields the atomic structure of materials and is based on the elastic scattering of X-rays from the electron clouds of the individual atoms in the system. The most comprehensive description of scattering from crystals is given by the dynamical theory of diffraction [29]. Powder XRD is a technique used to characterize the crystallographic structure, crystallite size (grain size) and preferred orientation in polycrystalline or powdered solid samples.

This technique has been used to examine the structure of the films grown on silicon nitride coated Si wafer substrates. Scanning the samples from 30° to 65° on a Bragg-Brentano configuration [1]. All XRD examinations were performed using a Philips X'Pert X-ray Diffractometer and line focus the Cu K_α source at 1.54 nm.

3.2.2 Nanoscale characterization

Transmission electron microscopy (TEM) is a microscopy technique [30] whereby a beam of electrons is transmitted through an ultra thin specimen, interacting with the specimen as it passes through. An image is formed from the interaction of the electrons transmitted through the specimen; the image is magnified and detected by a sensor like a CCD camera such as in our case.

The TEMs are capable of imaging at a significantly higher resolution than light microscopes, owing to the small De Broglie wavelength of electrons. It makes possible to examine in fine detail even as small as a single column of atoms, which is tens of thousands times smaller than the smallest resolvable object in a

[1] The diffractometer is operated in reflexion mode. Then the sample is placed on one axis of the diffractometer and tilted by an angle θ while a detector rotates around it on an arm at twice this angle 2θ.

light microscope. TEM forms a major analysis method in a range of scientific fields, in both physical and biological sciences.

This technique has been used to observe planar and cross section images of the samples just to determine the structure of CoO thin films from 1 to 20 nm grown on TEM windows and membrane based devices. No preparation is needed for planar observations, but after them, the samples are sandwitched using PELCO® Eponate 12™Kit with BDMA and then cuted into slices by means of a Leica EM UC6 ultramicrotome. The characterization has been performed on a Jeol JEM-2011 (Figure 3.2) with a resolution between 0.14 - 0.19 nm, operated at 200 kV, with a Gatan 794 MSC 600HP CCD camera.

Figure 3.2: Transmission electron microscope Jeol JEM-2011.

Moreover, TEM may be combined with other techniques. In this study, our TEM setup has installed also an electron diffractometer (ED) and an energy dispersive X-ray spectrometer (EDS) microanalysis INCA.

Electron diffraction via the transmission electron microscope is a powerful method for characterizing the structure of materials, including perfect crystals and defect structures. This technique is similar to X-ray and neutron diffraction, where the matter is irradiated by electrons and the results are obtained by observing the interference pattern. The advantages of electron diffraction over other methods, e.g., X-ray or neutron, arise from the extremely short wavelength ($\approx$ 2 pm), the strong atomic scattering, and the ability to examine tiny volumes of matter ($\approx$ 10 nm^3).

The EDS, or also called EDX, is an analytical technique used for the elemental analysis or chemical characterization of a sample. The principle of this technique is based on that each element emits characteristic X-rays whose correspond uniquely to that element. To stimulate the emission of this characteristic X-rays from a sample, a high-energy beam of charged particles (electrons in our case) is focused into the sample. At rest, an atom within the sample contains ground state electrons in discrete energy levels or electron shells bound to the nucleus. The incident beam may excite an electron in an inner shell, ejecting it from the shell while creating an electron hole where the electron was. An electron from an outer higher-energy shell then fills the hole, and the difference in energy between the higher-energy shell and the lower energy shell may be released in the form of a characteristic X-ray. The number and energy of these X-rays emitted from the sample can be measured by an energy-dispersive spectrometer. This technique is very useful when the samples are very small or thin, when they are not observable by imaging. Then the EDS may assure that the beam of electrons is pointing to the sample.

As a result of the weakness of the magnetic signal, the critical phenomena in antiferromagnetic systems have been little studied by magnetic measurements despite its crucial importance in various effects previously mentioned. The recent availability of ultrahigh sensitivity specific heat equipment provides an alternative experimental technique to study the critical properties of these systems. In addition to the weakness of the magnetic signal, characterizing any antiferromagnet, a number of other reasons justify the use of specific heat measurements to study the critical behaviour of CoO. In oxide nanocrystals, uncompensated loosely coupled surface spins are often present. Although they represent a small fraction of the total number of magnetic moments in the sample, their magnetic signal dominates in magnetic susceptibility measurements and it may hide the weak magnetic signal characterizing the order-disorder transition at T_N. The first highly sensitive specific heat measurements performed on single ultrathin layers (from 1 to 20 nm) of antiferromagnetic CoO nanograins are reported. The measurements of the thermodynamic properties of such small size samples (the sample total mass is less than 10 ng) has been made possible by the use of a cutting edge nanocalorimetry technique, providing ultrahigh sensitivity in a broad temperature range. From these measurements, the Néel temperature is extracted.

The quasiadiabatic nanocalorimetry is a characterization technique specialized on measuring the heat capacity of very tiny samples, essentially thin films or nanosamples. Note that heat capacity is a fundamental thermodynamic magnitude, and from the magnetic point of view, it reports information on the evolution of the magnetic entropy on the sample. Thus, in the presence of the order-disorder transition typically appears an abrupt jump on the heat capacity signal.

Typically, the sensitivity of the quasi-adiabatic nanocalorimetry enables the measurement of phase transitions on samples of few picograms. Nevertheless, to measure them, the sample should be placed on the calorimetric cell (a silicon

nitride substrate) of microfabricated nanocalorimeter. For that, for all the CoO thicknesses deposited simultaneously to the growth on the test substrate, identical samples were deposited onto the nanocalorimetric devices using a microfabricated shadow mask to localize them on the calorimetric cells. All the measurements shown in this project has been performed using calorimetric setup developed by the Group of Nanomaterials and Microsystems (GNaM) [32]. The vacuum chamber of the EB-PVD is equipped to permit *in-situ* experiments after deposition of the samples, in a base pressure of $2 \cdot 10^{-6}$ mbar, and therefore avoid ambient exposition of the samples, preventing their contamination. The experiment is realized starting the measurements at 100 K up to 400 K with a heating rate of $6 \cdot 10^4$ K/s.

Chapter 4

Results and discussion

4.1 Growth optimization of bulk cobalt oxide (II)

As mentioned in the previous section, we have used a trial and error procedure, when we fix the deposition conditions (partial pressure of oxygen and substrate temperature), a thick (bulk-like) film of 60 nm is evaporated. Subsequently, the samples are characterized using XRD and after discussing about the results, the new deposition conditions are decided. Following that procedure, several cycles were necessaries to obtain the desired CoO salt rock structure (Table 4.1).

Sample	**Substrate temperature (K)**	**Partial pressure (mbar)**	**Structure obtained**
b	525	$8.0 \cdot 10^{-4}$	CoO (SR) (111) textured
c	475	$5.0 \cdot 10^{-4}$	CoO (SR + ZB)
d	575	$5.0 \cdot 10^{-4}$	CoO (SR) + Co_3O_4
e	525	$2.5 \cdot 10^{-4}$	CoO (SR)

Table 4.1: Evaporation conditions for every test sample and results obtained from XRD diffractogram.

The study is started fixing deposition conditions at 525 K and $8.0{\cdot}10^{-4}$ mbar. The sample obtained had a poor crystallinity and is not very well defined; nevertheless, peaks corresponding to the CoO SR type can be identified. It shows a high texture on (111) planes. For the next sample (*c*), the temperature and partial pressure of oxygen are reduced. The resulting film exhibits a large polycrystallinity of the CoO salt rock phase, but mixed with a certain amount of the zinc blende (ZB) structure which is identified by the peak located at 34.6 degrees (see Appendix B). In sample (*d*), with the intention to erase the metastable phase, the temperature is raised up to 575 K obtaining both the CoO SR type and the Co_3O_4 phase. The Co_3O_4 cubic structure can be identified by the peak placed at 36.8º which is indexed as the family of planes (311) (see Appendix D). Finally, the sample (*e*) corresponds to a polycrystalline and non-textured layer of CoO salt rock type, where the reduction in temperature and partial pressure of oxygen avoids the formation of the Co_3O_4 structure.

In Figure 4.1 the theoretical diffraction pattern for CoO SR structure (a, refer to Powder Diffraction File (PDF) in Appendix A) is compared to the corresponding four different samples (b to e) where the contribution of the substrate has been subtracted. In that figure, we can observe the evolution of the trial and error procedure finishing in the CoO SR structure on the sample (*e*).

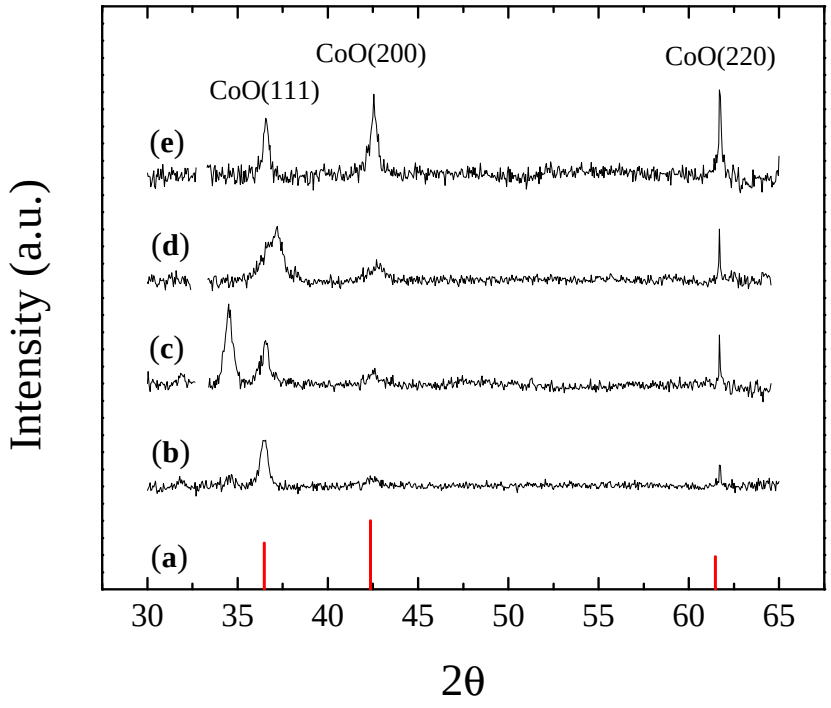

Figure 4.1: XRD diffractograms for theoretical CoO salt rock structure (a) and for different samples (from b to e). The diffraction patterns have been normalized respect to the maximum intensity value and the baseline correction has been applied. The (111), (200) and (220) reflections corresponding to CoO SR structure are indexed.

4.2 Growth and characterization of ultra thin films

As described in previous section, with deposition conditions well defined, a series of samples with thicknesses ranging from 1 to 20 nm have been prepared onto SiN_X TEM windows with the aim to determine the microstructure evolution with thickness growth.

4.2.1 Transmission electron microscopy plane view

For the sample of 1 nm (Figure 4.2 left) no crystalline structure is observed. The film is too thin for the microscope resolution taking into account the CoO density. Besides, the ED pattern give no signal of crystallinity, the halo corresponds to the amorphous contribution for CoO film and SiN_X membrane. In spite of this, the energy-dispersive X-ray spectroscopy (EDS) analysis shows the presence of cobalt, i.e., the analysis has been performed over the deposited film.

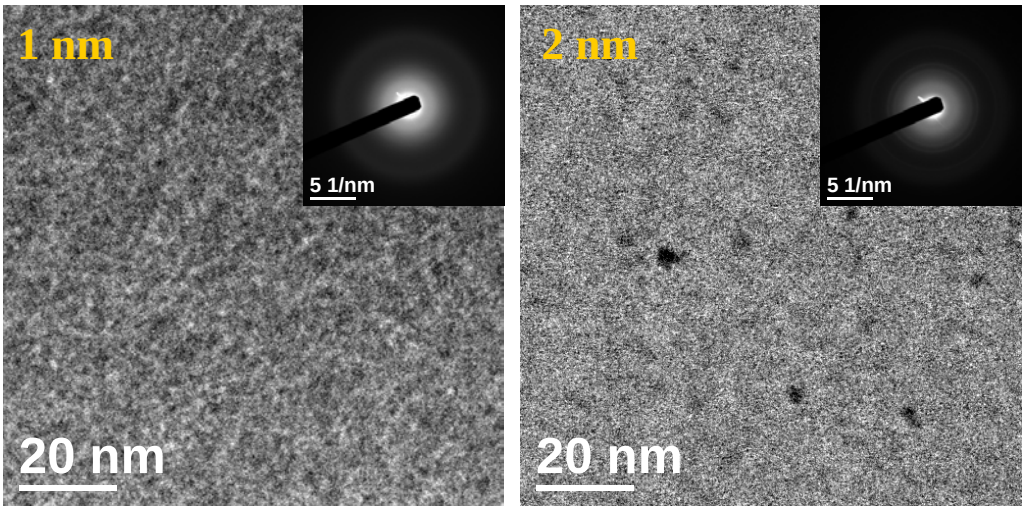

Figure 4.2: TEM plane view image for 1 nm CoO sample at 200.000 X (left) and for 2 nm CoO sample at 200.000 X (right). The corresponding ED captures are included for every image (insets).

When the film thickness reaches the 2 nm something changes (Figure 4.2 right). The image taken with the CCD camera is different to the previous one, but there are no observable grains yet. By other hand, the ED rings show an incipient crystallinity which may correspond with the CoO salt rock structure patterns.

An important fact occurs when the film thickness achieve the 3 nm thick. For first time the image (Figure 4.3 left) shows the presence of grains with their bound-

aries well defined. And the ED rings match perfectly with the three most intense peaks for the CoO salt rock type (see Appendix A). From that thickness on, the grains increase their diameter with films thicknesses, higher the thickness higher the polygonal shape of the grains.

The ED rings for all the samples also show the corresponding patterns for the desired CoO SR type, as well as that samples are completely polycrystalline (Figure 4.4).

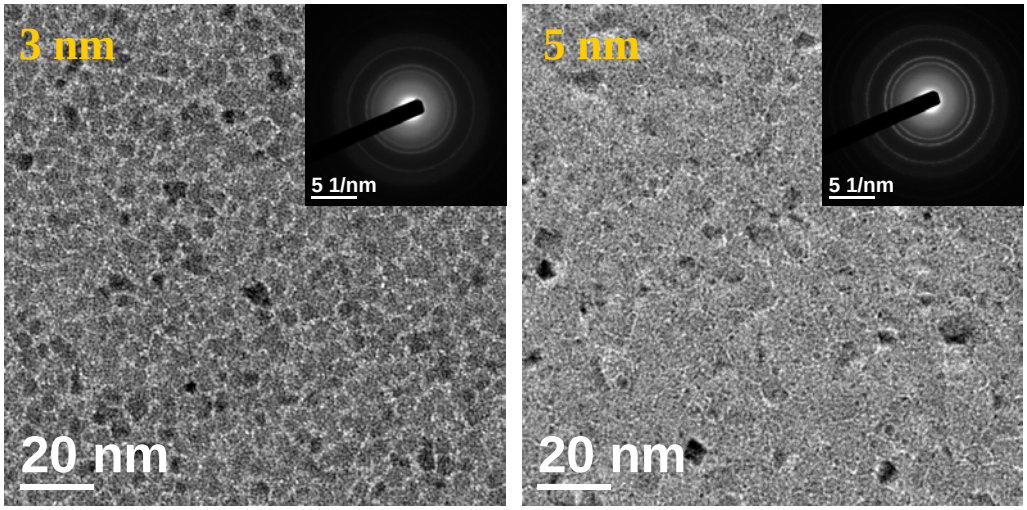

Figure 4.3: TEM plane view image for 3 nm CoO sample at 150.000 X (left) and for 5 nm CoO sample at 150.000 X (right). The corresponding ED captures are included for every image (insets).

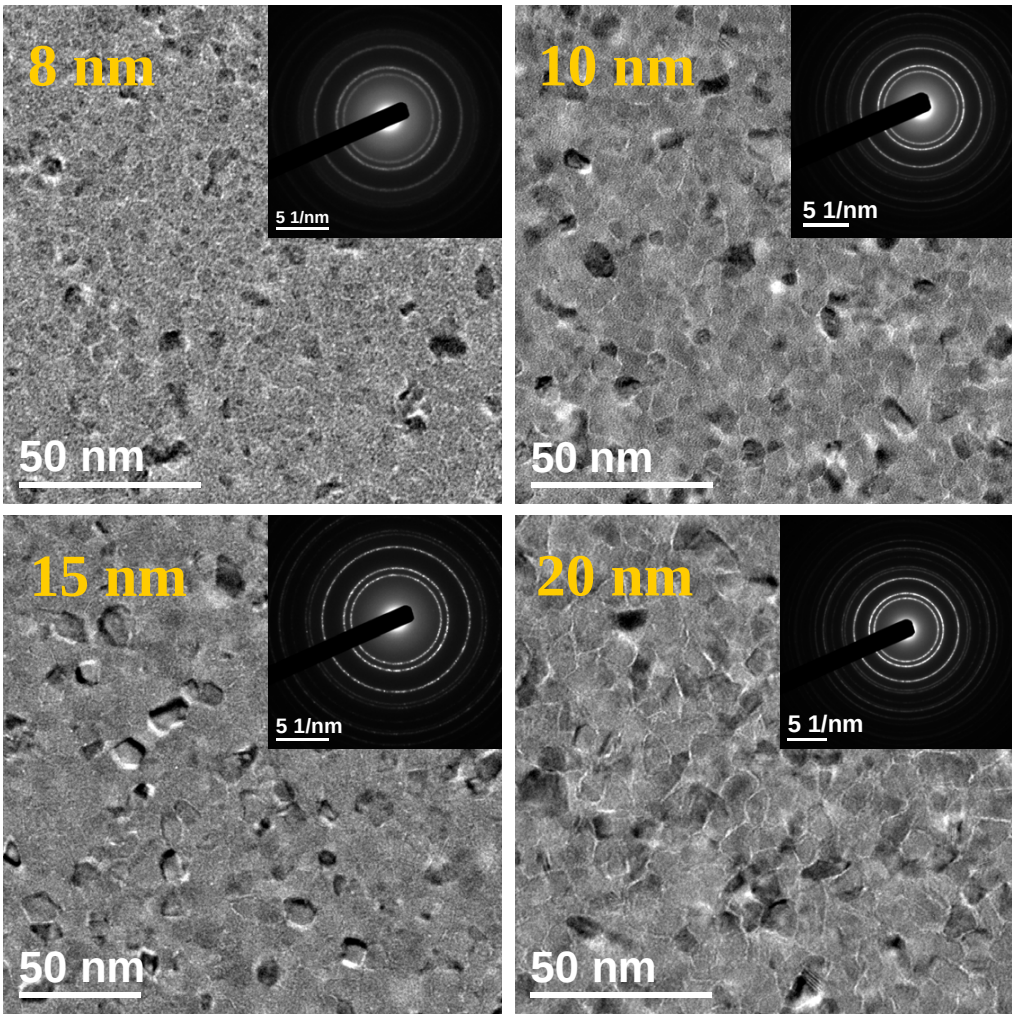

Figure 4.4: TEM plane view image for 8 nm CoO sample at 150.000 X (top-left), for 10 nm CoO sample at 150.000 X (top-right), for 15 nm CoO sample at 100.000 X (bottom-left) and for 20 nm CoO sample at 150.000 X (bottom-right). The corresponding ED captures are included for every image (insets).

The obtaining of a narrow dispersion on the size distribution of the grains is quite interesting due to the dependence of the magnetic behaviour with the microstructure, as explained on Chapter 1. So that, for the films of 3, 5, 8, 10, 15 and 20 nm thick a digital counting has been done with the intention to calculate de mean grain diameter for every thickness (Figure 4.6). The number of grains counted for every sample has been taken to keep constant the statistical error [1].

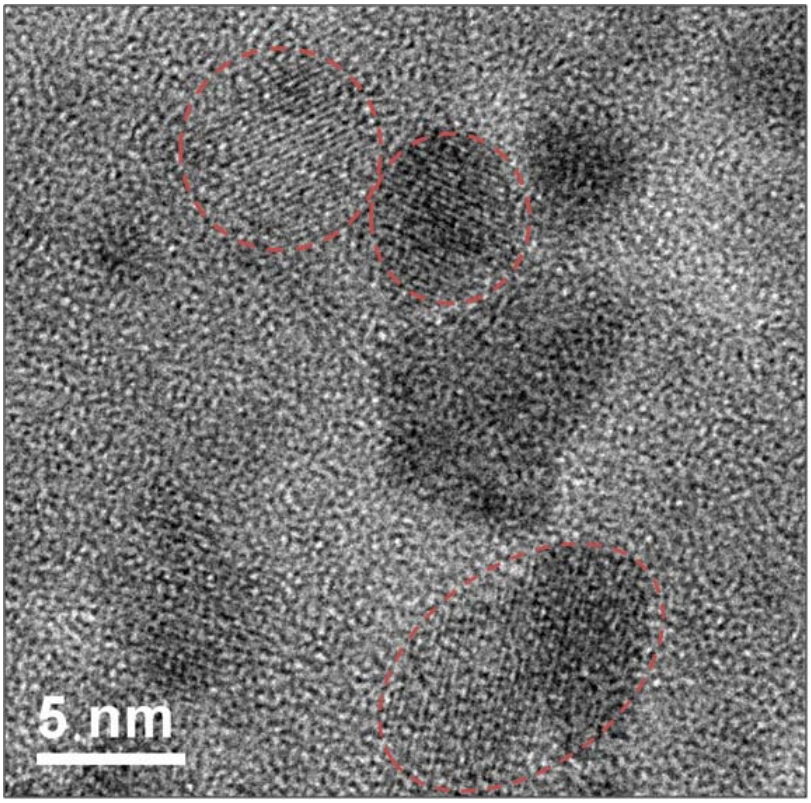

Figure 4.5: HRTEM image for 5 nm CoO sample where different crystall orientations are indicated (red dashed line).

After the *in-plane* study, it results clear that the films are formed by circular

[1]The number of samples (N) needed is determined when the 68.2 % of them show a deviation of $\pm\,\sigma = \left[\frac{1}{N}\sum_{n=1}^{N}(X_i - \bar{X})\right]^{1/2}$.

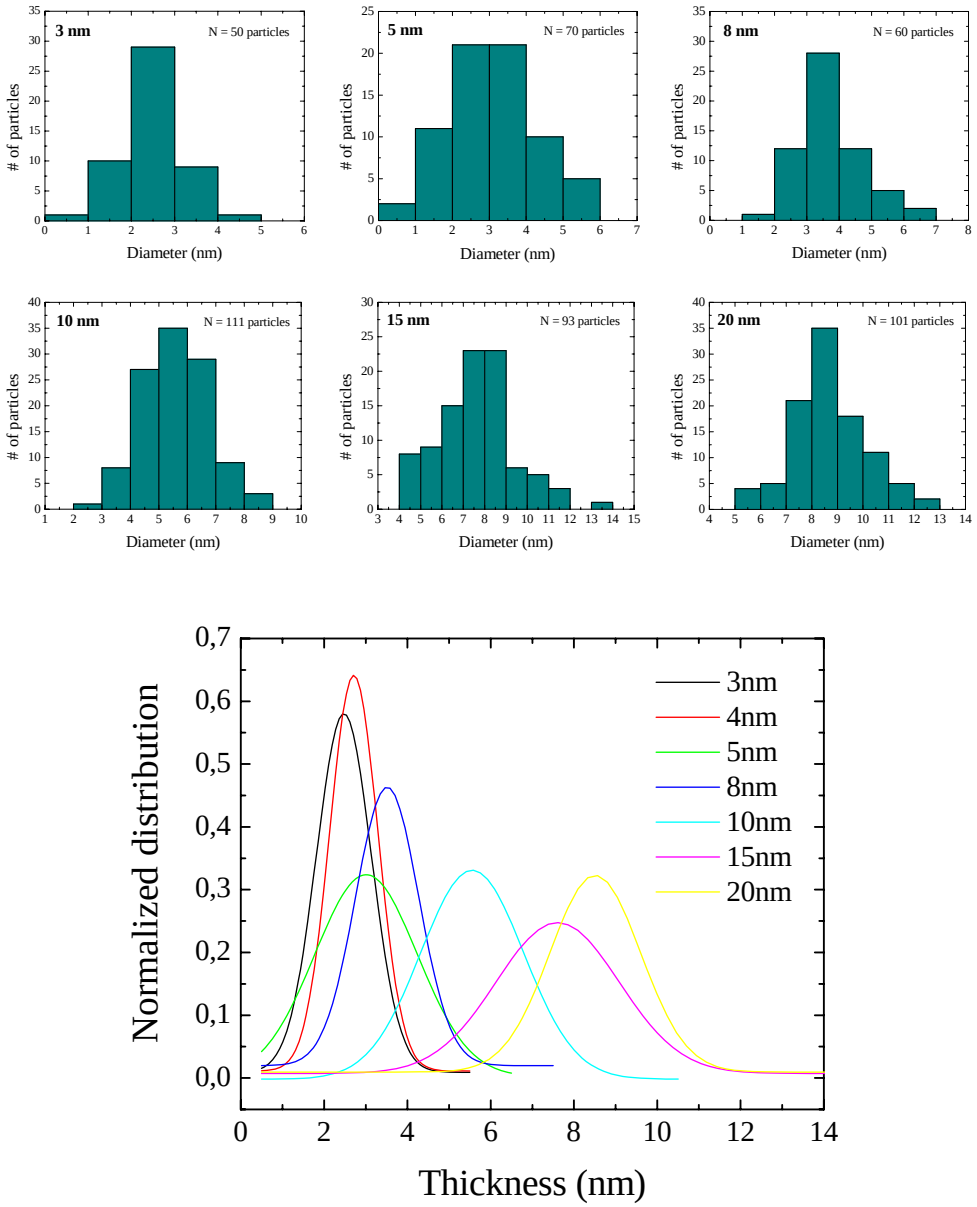

Figure 4.6: The six upper small graphs represent the number of particles respect to the diameter for films with different thicknesses. Every distribution uses a different number of samples (N). The lower graph shows a gaussian fitting for the grains diameter distribution versus the thickness of the films.

grains with polygonal shape. Is observed also that within grain boundaries exists a region where the crystallographic order should disappear due to the different orientation of nanograins, as can be seen in high resolution transmission electron microscopy (HRTEM) image showed in Figure 4.5.

4.2.2 Transmission electron microscopy cross section

With the *in-plane* characterization finished, is needed to know the shape of the grains *out-plane* by means of a cross section study. *A priori* there are two possibilities, spherical or columnar growth, then, is preferred the columnar growth because this fact maximizes the volume of the nanograins, i.e., the magnetic arrangement. Following the procedure described in Chapter 3, two different samples

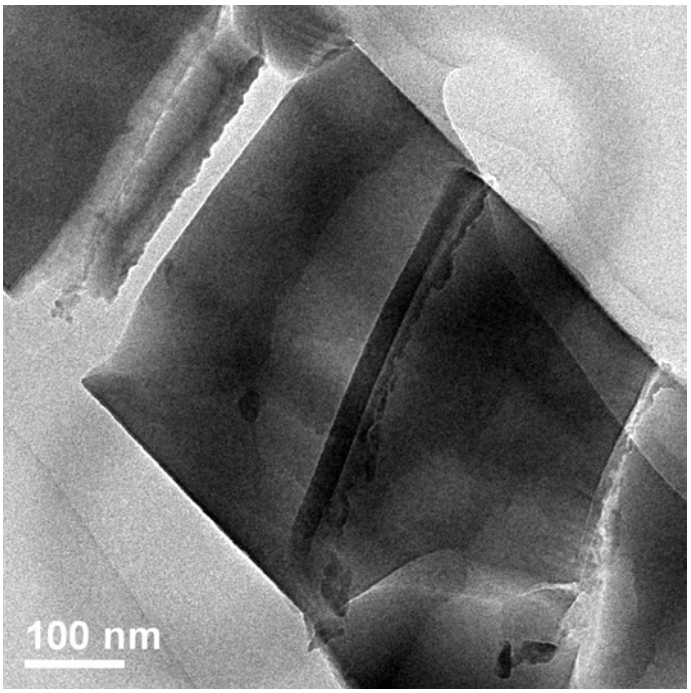

Figure 4.7: TEM cross section image for 2 nm CoO sample. The dark zone corresponds to a 180 nm SiN_X membrane and CoO thin film is placed at lower border but it is indistingible at 30.000 X.

are studied; the first one is a 2 nm CoO thick film (Figure 4.7), prepared with the aim to know what happens before the 3 nm of thickness when no grains are observed. The second sample is a 20 nm CoO thick film (Figure 4.9) grown for observe the microstructure of the film at the final thickness.

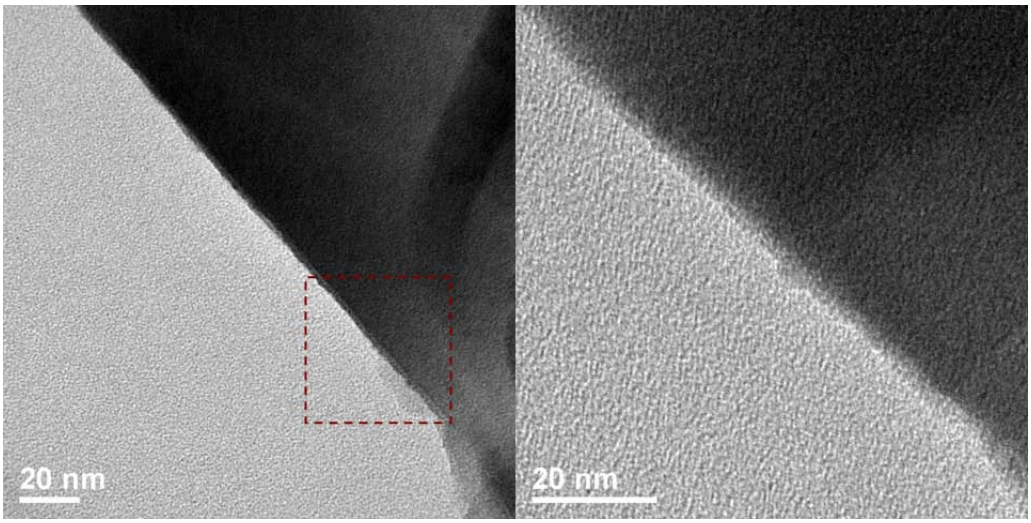

Figure 4.8: TEM cross section image for 2 nm CoO sample at 120.000 X. The dark zone corresponds to the SiN_X membrane and CoO thin film is placed within the border (left). Zoom in (red dashed zone) TEM cross section image for 2 nm CoO sample at 250.000 X. The dark zone corresponds to the SiN_X membrane and CoO thin film is placed within the border (right).

Increasing the magnification from the Figure 4.7, the Figure 4.8 shows that with 2 nm thickness the film is continuous and also that no grains are formed. We can conclude that below 3 nm most of the sample is still amorphous.

In Figure 4.9, we can observe the 20 nm thin film TEM cross section image. It shows how the CoO film is deposited following a columnar growth with the surface quite smooth. There are some irregularities which can be related with the ultramicrotomy (cutting process).

On Figure 4.10 the same image is compared in bright field (BF) and dark field (DF). In the BF image the roughness of the surface is clearer observable and smooth, whereas the grain boundaries are visible, although not better than in the *in-plane* characterization. In this case due to the depth of the sample a lot of nanograins are superposed diffusing the contrast of the image.

In the DF image (Figure 4.10 right) only one orientation is showed as can be seen by bright grains, which verifies that CoO films are polycrystalline.

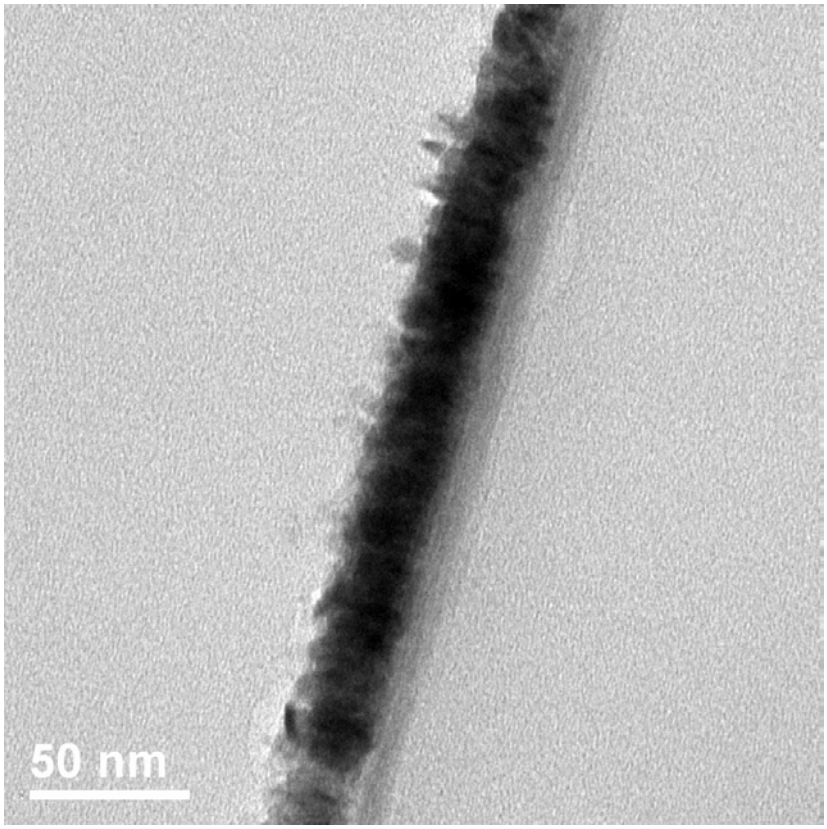

Figure 4.9: TEM cross section image for 20 nm CoO sample at 80.000 X. The dark zone corresponds to a CoO film and the right medium gray film is a 20 nm SiN_X membrane. The light gray belongs to the stacking polymer.

At high resolution we can observe how the columns height corresponds to the

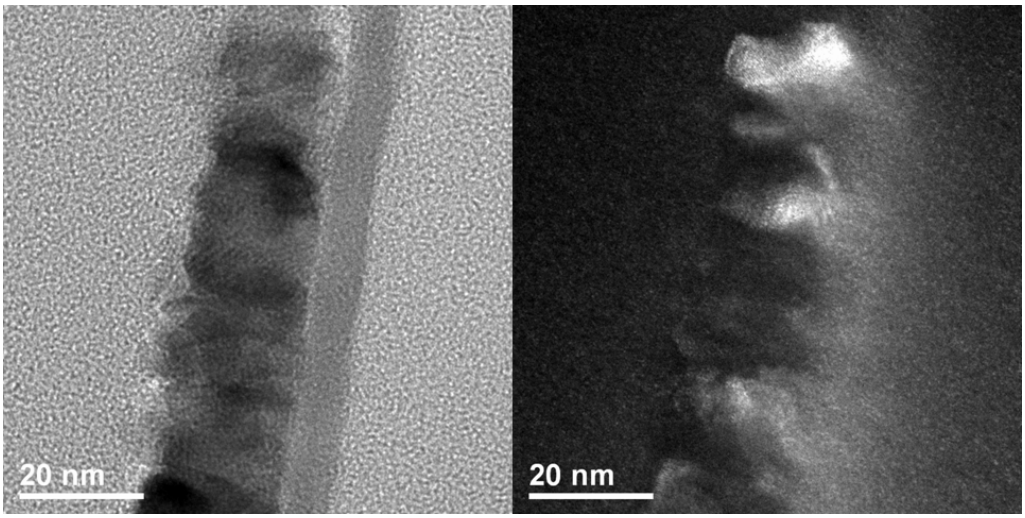

Figure 4.10: TEM cross section image for 20 nm CoO sample at 250.000 X in bright field (left) and in dark field (right).

thickness of the film. Most of the columns have a conical shape (Figure 4.11) due to the different growth velocity of the three different families of planes present on the samples, which promotes the appearance of impingement during the growth. Nevertheless, they can be treated in average as columns. The first 2 or 3 nm of amorphous or non-crystalline CoO (light gray) can be also seen close to the SiN_X membrane (medium gray at right border of the image).

Analyzing the ED rings on Figure 4.12 there are differences respect to previous ED captures from *in-plane* characterization (Figure 4.4 bottom-right inset). In this case, instead of well defined rings, there are bright points over the form of previous ones. This fact is due to the quantity of mass involved in diffraction process and to the polycrystalline nature of the sample. By other hand, measuring the three first rings, the interplanar distances can be converted to the double of the angular diffraction position (2θ) giving 34.94º, 40.70º and 58.46º. These peaks are displaced to the left respect to theoretical positions for CoO SR structure (see Appendix A) with an error around 5%. The fact that the displacement is always

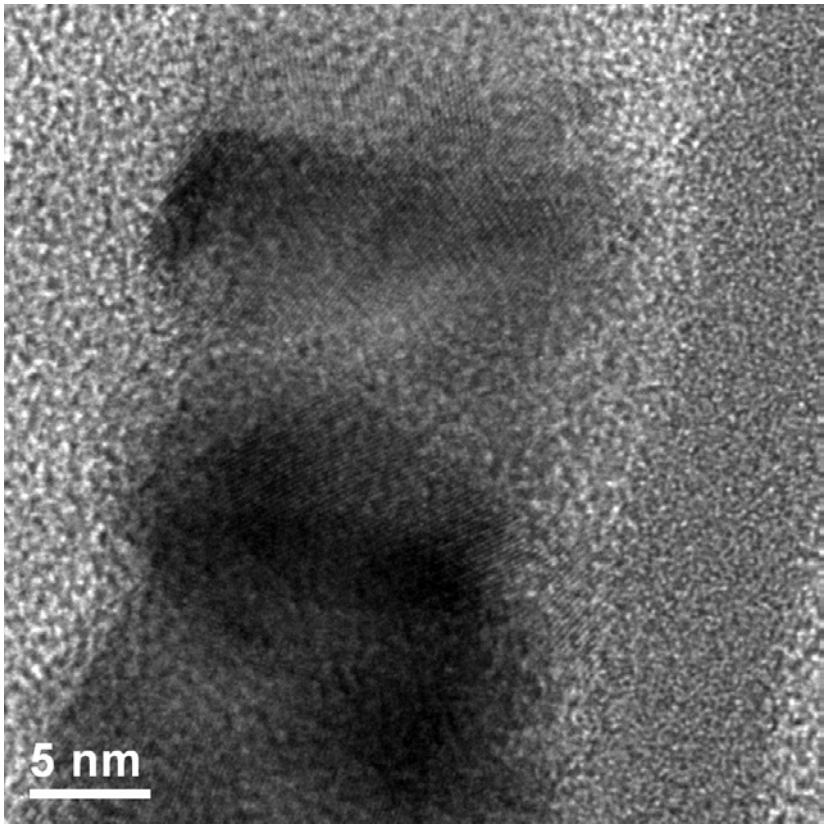

Figure 4.11: HRTEM cross section image for 20 nm CoO sample at 600.000 X.

constant in same sense confirms that there is any kind of error related to the measure: instrumental or systematic. Despite, the results confirms that the sample shows the CoO SR structure.

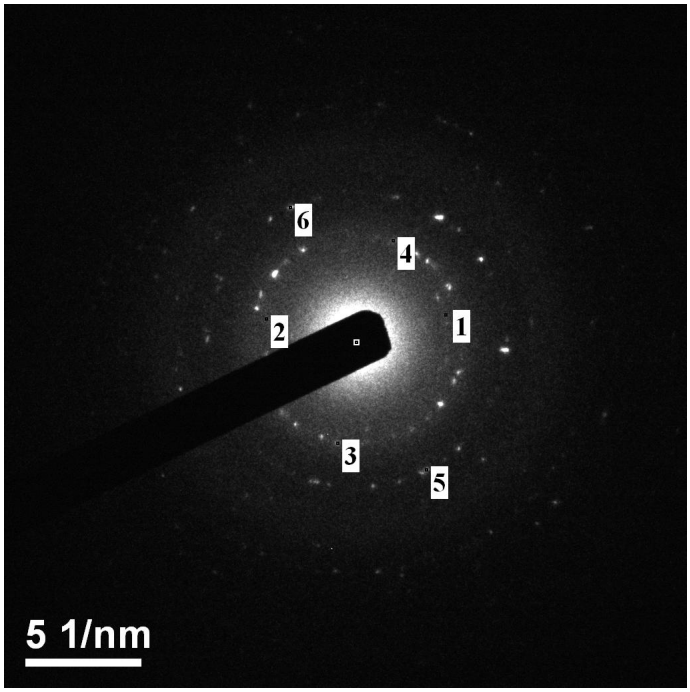

Figure 4.12: ED capture corresponding to a cross section of 20 nm CoO sample. There are indexed three rings in couples of two points with interplanar averaged distances of d_{1-2} = 2.566 Å, d_{3-4} = 2.215 Å and d_{5-6} = 1.578 Å.

Summarizing the results obtained after the morphological characterization. The Figure 4.13 shows the dependence of grain size *in-plane* and *out-plane* as a function of nominal thickness. This graph clarifies the growth evolution of the nanograins: how their height has a constant relation with nominal thickness, whereas the width seems to grow more slowly, with difficulty. Therefore, it exists an inhomogeneous columnar growth due to the impingement between grains, that is originated by the growth velocity of each family of planes.

The non crystallinity during the first nanometres of growth is due to the amorphous nature of the substrate and to the superficial stress on the CoO layer. Similarly, on the surfaces of the nanograins the large stress breaks the crystallinity.

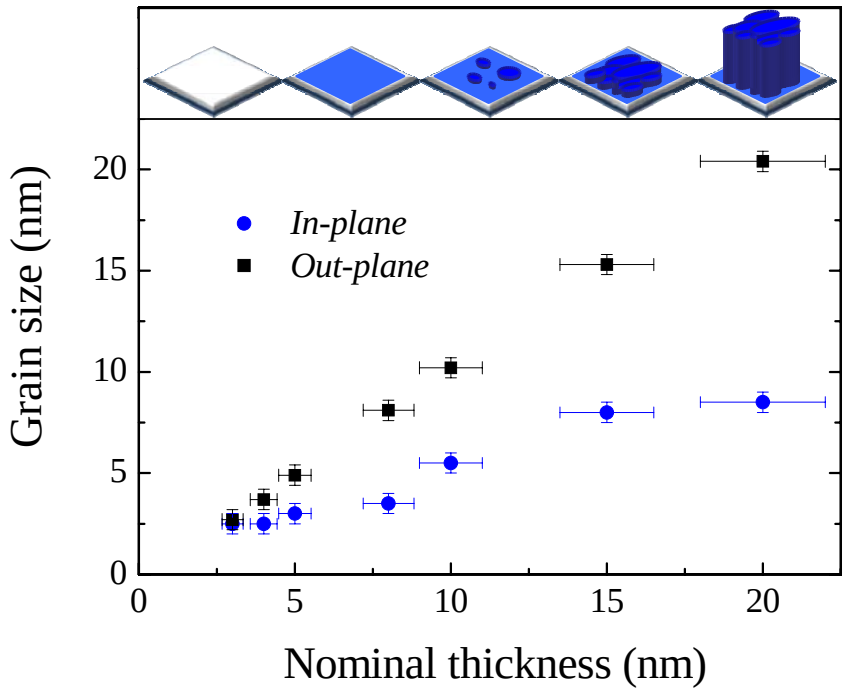

Figure 4.13: Grain size *in-plane* and *out-plane* respect to the nominal thickness. The inset shows schematics of the grains structure evolution with film thickness.

4.3 Quasiadiabatic nanocalorimetry

Different samples of CoO are measured using the quasi-adiabatic nanocalorimetry technique described on Chapter 3. If previous conclusions are right, below T_N the sample must suffer a structural contraction to the tetragonal phase, which one shows AF behaviour, and heating it up again at a heating rate about 60.000 K/s will return to the PM state of the SR structure.

The results of this experiment are showed in Figure 4.14 and where the magnetic transition is clearly observed for each thickness. The slopes of the curves before and after the transition are different, which agree with the Debye model for the specific heat contributions of two different materials [2], i.e., they are the corresponding contributions to the CoO tetragonal phase (space group I4/mmm) before the magnetic transition and to the CoO salt rock type with cubic phase (space group $Fm\bar{3}m$) after it.

The specific heat increases monotonously with temperature (see Figure 4.14), as expected for a dominant lattice contribution. An additional contribution develops as one goes from thin to thick films, which represents the sample magnetic specific heat. The Néel temperature is taken as the temperature at which the inflexion of the specific heat curve occurs. The T_N value and the specific heat jump occurring at transition temperature decrease with decreasing sample thickness.

The knowledge and characterization of this depression is of crucial importance for technological applications, since if the microstructure affects the magnetic properties, the temperature determines if the material is antiferromagnetic or not. The measure reports a value of $T_N \approx 290\ K$ for the thicker sample which corresponds with the bulk values reported previously in Chapter 1.

[2] In solid state physics, the Debye model is a method developed for estimating the phonon contribution to the heat capacity in a solid: $c_v = \frac{12\pi^4}{5} n k_B \left(\frac{T}{\Theta_D}\right)^3$ where $\Theta_D = \frac{\hbar c}{k_B} \sqrt[3]{6\pi^2 n}$ depends on every material. It treats the vibrations of the atomic lattice (heat) as phonons in a box.

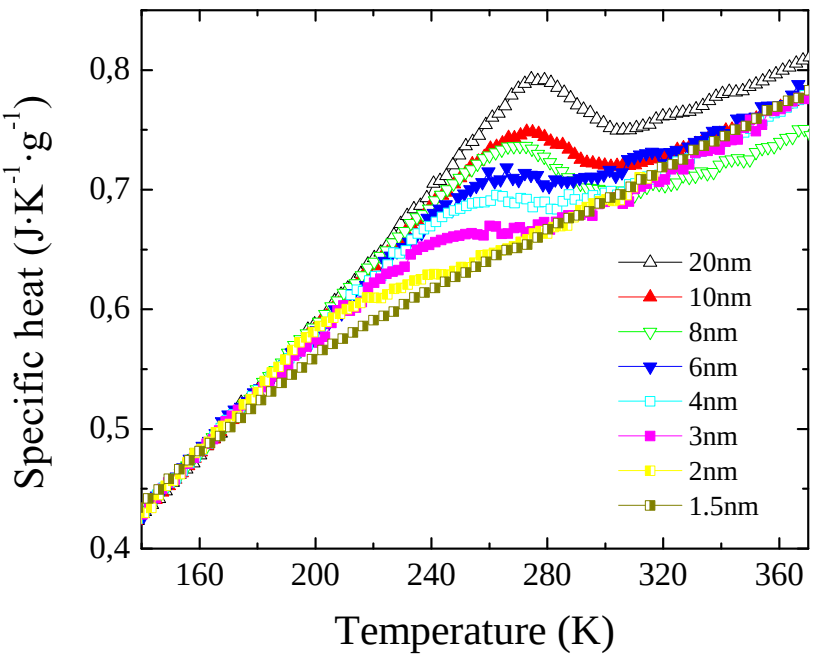

Figure 4.14: Specific heat as a function of temperature for samples of CoO with thicknesses from 1.5 of 20 nm measured by means of quasi-adiabatic nanocalorimetry technique.

Chapter 5

Project cost

At the end of this Final Career Project, a study of costs has been realized with the aim to quantize the amount of money spent.

Taking into account the price of materials used as substrates, products used to prepare de samples, renting of equipment for characterization and labour time; the total project cost has reached **10100 €**. In this calculation there are some exclusions as the electricity consumed and the use of laboratories or installations belonging to the university as the cleaning room. All costs are showed in detail on Table 5.1.

Quantity	**Item**	**Unit cost (€)**	**Total cost (€)**
2	Ethanol, 99+% 1 L	21.80	43.60
1	2-propanol, 99+% 2500 mL	37.90	37.90
1	Acetone, 99+% 2500 mL	32.40	32.40
1	Silicon nitride wafer 4”	30.00	30.00
20	Silicon nitride windows for TEM	42.00	840.00
2	Membrane based devices	50.00	100.00
1	Cobalt pellets 99.95%, 50 g	103.50	103.50
30	CoO evaporation	60.00	1800.00
40	Liquid nitrogen 1 L	2.50	100.00
20	XRD sample analysis	20.00	400.00
40	TEM sample characterization	29.00	1160.00
140	Labour time	30.00	4200.00
20	Supervision	60.00	1200.00
	TOTAL PROJECT COST	**=**	**10047.40**

Table 5.1: Project cost.

Chapter 6

Conclusions

In this project a methodology to obtain the cobalt oxide (CoO) salt rock structure in thin film form has been developed using electron beam physical vapor deposition on reactive atmosphere electron beam evaporation (EB-PVD). The optimized conditions have been found through a trial and error procedure, depositing bulk (60 nm thick) samples with given conditions and verifying the phase obtained by X-ray diffraction (XRD) technique. It has been found that when evaporating cobalt (Co) atoms from a metallic target at a rate of 1 Å/s under an oxygen rich atmosphere, with oxygen partial pressure of $2.5 \cdot 10^{-4}$ mbar the correct stoichiometry and crystalline phase have been obtained when substrate temperatures is rose up to 525 K.

Once the optimal conditions have been verified, a set of ultra thin film samples with thicknesses ranging from 1 to 20 nm has been grown. Using nanoscale characterization technique, transmission electron microscopy (TEM) together with electron diffraction (ED) and energy dispersive X-ray spectroscopy (EDS), we have observed the CoO microstructure evolution for the different growth steps, from the beginning of the growth up to bulk dimensions. Initially the CoO is deposited showing an amorphous structure, then between 2 and 3 nm of thickness it

crystallizes and a granular organization can be observed. From this point, when the film increases its thickness the grains do that also in z-axis direction, but the impingement on *in-plane* direction prevents a spherical growth, instead of that, the film shows a columnar growth.

Finally, the preliminary results, on using the quasi-adiabatic nanocalorimetry to inspect the antiferromagnetic to paramagnetic transition, permit to observe a clear dependence of the phase transition with the CoO layer grains size. The Néel temperature of CoO suffers a big depression with size, thing that should condition the future technological applications.

The next step lies in the study of magnetic properties of Co/CoO exchange bias (EB) systems, and their microstructure characterization to establish how it affects the magnetic exchange between antiferromagnetic (AF) and ferromagnetic (FM) layers.

Bibliography

[1] T. Ambrose and C. L. Chien, *Phys. Rev. Lett.*, **76**, 1743-1746 (1996)

[2] K. Takano, R. H. Kodama, and A. E. Berkowitz, *Phys. Rev. Lett.*, **79**, 1130-1133 (1997)

[3] V. Skumryev, S. Stoyanov, Y. Zhang, G. Hadjipanayis, D. Givord and Josep Nogués, *Nature*, **423**, 850-853 (2003)

[4] Y. J. Tang, D. J. Smith, B. L. Zink, F. Hellman and A. E. Berkowitz, *Phys. Rev. B*, **67**, 054408 (2003)

[5] P. Grünberg, R. Schreiber and Y. Pang, *Phys. Rev. Lett.*, **57**, 2442-2445 (1986)

[6] M. N. Baibich, J. M. Broto, A. Fert, F. Nguyen Van Dau and F. Petroff, *Phys. Rev. Lett.*, **61**, 2472-2475 (1988)

[7] W. H. Meiklejohn and C. P. Bean, *Phys. Rev.*, **105**, 904-913 (1957)

[8] J. Nogués and I. K. Schuller, *J. Magn. Magn. Mater.*, **192**, 203-232 (1999)

[9] P. Curie, *Ann. Chim. Phys.*, **5**, 289-405 (1895)

[10] P. Langevin, *Ann. Chim. Phys.*, **5**, 70-127 (1905)

[11] P. Weiss, *Comptes Rendus*, **143**, 1136-1149 (1906)

[12] P. A. M. Dirac, *Phys. Rev.*, **74**, 7817 (1948)

[13] W. Heisenberg, *Zeitschrift für Physik*, **38**, 411-426 (1926)

[14] L. Néel, *C. R. Acad. Sc.*, **203**, 304-306 (1936)

[15] L. Néel, *Ann. Phys.*, **3**, 137-198 (1948)

[16] W. L. Roth, *Phys. Rev.*, **110**, 1333 (1958) and **111**, 772 (1958)

[17] M. M. Farztdinov, *Sov. Phys. Usp.*, **7**, 855 (1965)

[18] M. D. Rechtin and B. L. Averbach, *Phys. Rev. Lett.*, **26**, 1483 (1971), and references therein.

[19] B. D. Cullity, *Introduction to Magnetic Materials*, p. 157, Addison-Wesley, ISBN 978-0471477419 (1972)

[20] F. J. Romero, J. Jiménez, J. Del Cerro, *J. Magn. Magn. Mater.*, **280**, 257-263 (2004)

[21] M. Massot, A. Oleaga and A. Salazar, *Phys. Rev. B*, **77**, 134438 (2008)

[22] D. Bloch, R. Maury, C. Vetter and W. B. Yelon, *Phys. Lett. A*, **49**, 354-356 (1974)

[23] N. N. Greenwood and A. Earnshaw, *Chemistry of the Elements*, 2^{nd} ed., Oxford Butterworth-Heinemann, ISBN 978-0750633659 (1997)

[24] P. W. Anderson, *"Exchange in insulators, superexchange, direct exchange and double exchange in magnetism"*, Vol. I, G. T. Rado and H. Suhl, eds., Academic Press, New York (1963)

[25] A. P. Ramírez, *Nature*, **421**, 483 (2003)

[26] A. F. Lopeandía, *"Development of Membrane-based Calorimeters to Measure Phase Transitions at the Nanoscale"*, Thesis (2007)

[27] P. Patnaik, *Handbook of Inorganic Chemical Compounds*, McGraw-Hill, ISBN 978-0070494398 (2003)

[28] D. Wolfe and J. Singh, *Surf. Coat. Tech.*, **124**, 142–153 (2000)

[29] L. V. Azároff, R. Kaplow, N. Kato, R. J. Weiss, A. J. C. Wilson and R. A. Young, *X-ray diffraction*, McGraw-Hill (1974)

[30] B. Fultz and J. Howe, *Transmission Electron Microscopy and Diffractometry of Materials*, Springer, ISBN 978-3540437642 (2007)

[31] Ph. Buffat and J-P. Borel, *Phys. Rev. A*, **13**, 2287-2298 (1976)

[32] A. F. Lopeandía, F. Pi and J. Rodríguez-Viejo, *Appl. Phys. Lett.*, **92**, 122503 (2008)

Appendix A

Cobalt oxide (II) (salt rock type)

PDF

PDF Card

PDF Number	00-048-1719		**Status**	Primary	**Quality Mark**		Star (S)
Pressure/Temperature	Ambient						
Chemical Formula	Co O						
Weight %	Co78.65 O21.35						
Atomic %	Co50.00 O50.00						
Compound Name	Cobalt Oxide						
ANX							
Mineral Name							
Also Called							
Experimental	**Rad**	**λ**	**Filter**	**d-Spacing**	**Cutoff**	**Intensity**	**I/Ic**
	CuKá1	1.5406	Graph Mono	Diff.	2.6	Diffractometer	
	Camera Diameter	**Reference**					
	192	Kirik, S., Yakimov, I., Blochin, A., Soloyov, L., Inst. of Chemistry, Academy of Sciences, Krasnoyarsk, Russia. ICDD Grant-in-Aid (1997).					
Physical	**SYS**	**Space Group**	**Aspect**				
	Cubic	Fm-3m (225)					
	Author's Cell	**a**	**b**	**c**	**α**	**β**	**γ**
		4.2612 (1)					
		Volume					
		77.37					
	Reference	Visser, J. J. Appl. Crystallogr. 2, 89 1969).					
	Dcalc	**Dmeas**	**Dstruc**	**SS/FOM** F *8.0* =	**Melting Point**	**Z**	**R-factor**
	6.433			333 (0.003, 8.0)		4	
	Error						
Crystal	**Space Group**	**Z**	**Molecular Weight**				
	Fm-3m (225)	4	74.93				
	Crystal Cell	**a**	**b**	**c**	**α**	**β**	**γ**
		4.261	4.261	4.261	90	90	90
		Volume					
		77.37					
	Crystal Axial Ratio	**a/b**	**c/b**				

	Reduced Cell	**a**	**b**	**c**	**α**	**β**	**γ**
		3.013	3.013	3.013	60	60	60
		Volume					
		19.34					
Optical	**εα**	**nωβ**	**εγ**	**Sign**	**2V**		
	Reference						
Structure	**TF Type**						
	Origin						
	Atomic Coordinates	Atom	Num	Wyckoff	Symmetry	x	y	z	SOF	ITF	AET
	SG Symmetry Operators	Seq	Operator								
	Anisotropic Temperature Factors	Atom	Num	ATF11	ATF22	ATF33	ATF12	ATF13	ATF23		
Miscellaneous	**CAS Number**	1307-96-6									
	Pearson	cF8.00									
	Pearson w/o H										
	Subfile Indicator	Common Phase, Corrosion, Inorganic, Metals & Alloys, Primary Pattern									
	Prototype Structure	Na Cl									
	LPF Prototype Structure										
	Mineral Classification										
	Zeolite Classification										
	Entry Date	05/01/1997									
	Last Modification Date	01/24/2006									
	Former PDF #										
	Cross-Reference PDF #'s	00-002-1201 (Deleted), 00-009-0402 (Deleted), 00-043-1004 (Primary), 04-001-8626									
Comments	**Database Comments**										
	User Comments										
	Shared Comments										

d-Spacings

λ =1.54056

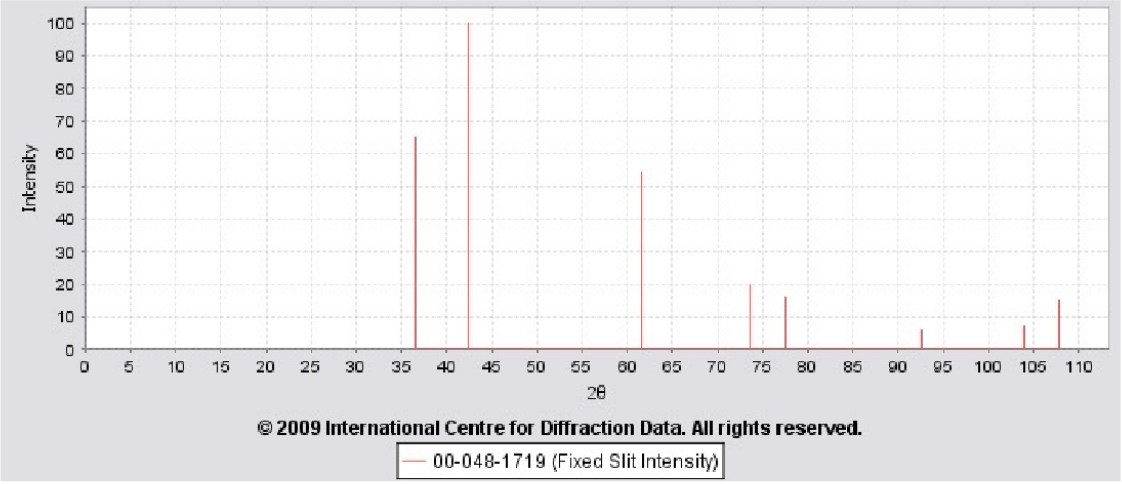

00-048-1719 (Fixed Slit Intensity)

2θ	d(Å)	Intensity	h	k	l
36.4919	2.4602	65	1	1	1
42.3865	2.1307	100	2	0	0
61.497	1.5066	54	2	2	0
73.6729	1.2848	20	3	1	1
77.5321	1.2302	16	2	2	2
92.6161	1.0653	6	4	0	0
103.9849	0.9776	7	3	3	1
107.8707	0.9529	15	4	2	0

Appendix B

Cobalt oxide (II) (zinc blende type) PDF

PDF Card

PDF Number	00-042-1300		**Status**	Primary	**Quality Mark**		Star (S)
Pressure/Temperature	Ambient						
Chemical Formula	Co O						
Weight %	Co78.65 O21.35						
Atomic %	Co50.00 O50.00						
Compound Name	Cobalt Oxide						
ANX							
Mineral Name							
Also Called							
Experimental	**Rad**	**λ**	**Filter**	**d-Spacing**	**Cutoff**	**Intensity**	**I/Ic**
				Calculated			
	Camera Diameter	**Reference**					
		Grimes, R., Fitch, A. J. Mater. Chem. 1, 461 (1991).					
Physical	**SYS**	**Space Group**	**Aspect**				
	Cubic	F-43m (216)					
	Author's Cell	**a**	**b**	**c**	**α**	**β**	**γ**
		4.544(3)					
		Volume					
		93.82					
	Reference	Ibid.					
	Dcalc	**Dmeas**	**Dstruc**	**SS/FOM** F *10.0* =	**Melting Point**	**Z**	**R-factor**
	5.305			1000(0, 10.0)		4	
	Error						
Crystal	**Space Group**	**Z**	**Molecular Weight**				
	F-43m (216)	4	74.93				
	Crystal Cell	**a**	**b**	**c**	**α**	**β**	**γ**
		4.544	4.544	4.544	90	90	90
		Volume					
		93.82					
	Crystal Axial Ratio	**a/b**	**c/b**				
	Reduced Cell	**a**	**b**	**c**	**α**	**β**	**γ**
		3.213	3.213	3.213	60	60	60
		Volume					
		23.46					

Optical	**εα**	**nωβ**	**εγ**	**Sign**	**2V**
	Reference				

Structure	**TF Type**	
	Origin	
	Atomic Coordinates	Atom | Num | Wyckoff | Symmetry | x | y | z | SOF | ITF | AET
	SG Symmetry Operators	Seq | Operator
	Anisotropic Temperature Factors	Atom | Num | ATF11 | ATF22 | ATF33 | ATF12 | ATF13 | ATF23
Miscellaneous	**CAS Number**	
	Pearson	cF8.00
	Pearson w/o H	
	Subfile Indicator	Corrosion, Inorganic, Metals & Alloys, Primary Pattern
	Prototype Structure	Zn S
	LPF Prototype Structure	
	Mineral Classification	
	Zeolite Classification	
	Entry Date	11/19/1991
	Last Modification Date	01/24/2006
	Former PDF #	
	Cross-Reference PDF #'s	04-002-2694
Comments	**Database Comments**	
	User Comments	
	Shared Comments	

d-Spacings

λ =1.54056

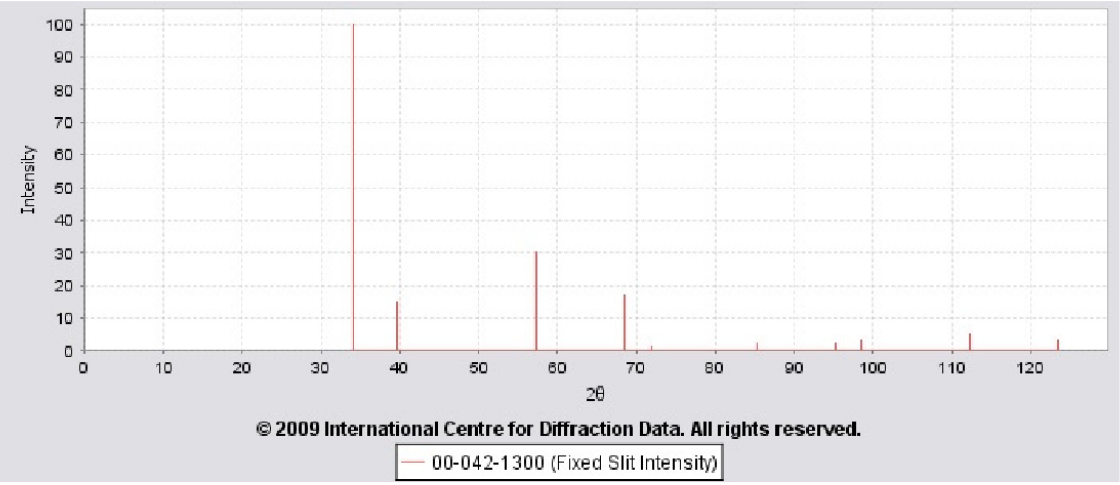

00-042-1300 (Fixed Slit Intensity)

2θ	d(Å)	Intensity	h	k	l
34.1481	2.6235	100	1	1	1
39.6358	2.272	15	2	0	0
57.2986	1.6066	30	2	2	0
68.4171	1.3701	17	3	1	1
71.9225	1.3117	1	2	2	2
85.385	1.136	2	4	0	0
95.2718	1.0425	2	3	3	1
98.5896	1.0161	3	4	2	0
112.2983	0.9275	5	4	2	2
123.4837	0.8745	3	5	1	1

Appendix C

Cobalt oxide (II) (wurtzite type)

PDF

PDF Card

PDF Number	01-089-2803		**Status**	Primary	**Quality Mark**		Indexed (I)
Pressure/Temperature	Ambient						
Chemical Formula	Co O						
Weight %	Co78.65 O21.35						
Atomic %	Co50.00 O50.00						
Compound Name	Cobalt Oxide						
ANX	AX						
Mineral Name							
Also Called							
Experimental	**Rad**	**λ**	**Filter**	**d-Spacing**	**Cutoff**	**Intensity**	**I/Ic**
	CuKá1	1.5406		Calculated	17.7	Calculated	3.82
	Camera Diameter	**Reference**					
		"Cobaltous Oxide with the Zinc Blende / Wurtzite-type Crystal Structure". Redman, M.J., Steward, E.G. Nature (London) 193, 867 (1962). Calculated from ICSD using POWD-12++.					
Physical	**SYS**	**Space Group**	**Aspect**				
	Hexagonal	P63mc (186)					
	Author's Cell	**a**	**b**	**c**	**α**	**β**	**γ**
		3.21		5.24			
		Volume					
		46.76					
	Reference	Ibid.					
	Dcalc	**Dmeas**	**Dstruc**	**SS/FOM** F *12.0* =	**Melting Point**	**Z**	**R-factor**
	5.322		5.321	1000(0, 12.0)		2	
	Error						
Crystal	**Space Group**	**Z**	**Molecular Weight**				
	P63mc (186)	2	74.93				
	Crystal Cell	**a**	**b**	**c**	**α**	**β**	**γ**
		3.21	3.21	5.24	90	90	120
		Volume					
		46.76					
	Crystal Axial Ratio	**a/b**	**c/a**				
			1.6324				
	Reduced Cell	**a**	**b**	**c**	**α**	**β**	**γ**
		3.21	3.21	5.24	90	90	120
		Volume					

		46.76			
Optical	**εα**	**nωβ**	**εγ**	**Sign**	**2V**
	Reference				

Structure	**TF Type**	
	Origin	
	Atomic Coordinates	Atom Num Wyckoff Symmetry x y z SOF ITF AET
	SG Symmetry Operators	Seq Operator
	Anisotropic Temperature Factors	Atom Num ATF11 ATF22 ATF33 ATF12 ATF13 ATF23

Miscellaneous	**CAS Number**	
	Pearson	hP4.00
	Pearson w/o H	
	Subfile Indicator	Corrosion, ICSD Pattern, Inorganic, Metals & Alloys, Primary Pattern
	Prototype Structure	Zn S
	LPF Prototype Structure	
	Mineral Classification	
	Zeolite Classification	
	Entry Date	12/16/2002
	Last Modification Date	01/25/2006
	Former PDF #	
	Cross-Reference PDF #'s	

Comments	**Database Comments**	
	User Comments	
	Shared Comments	

d-Spacings

λ =1.54056

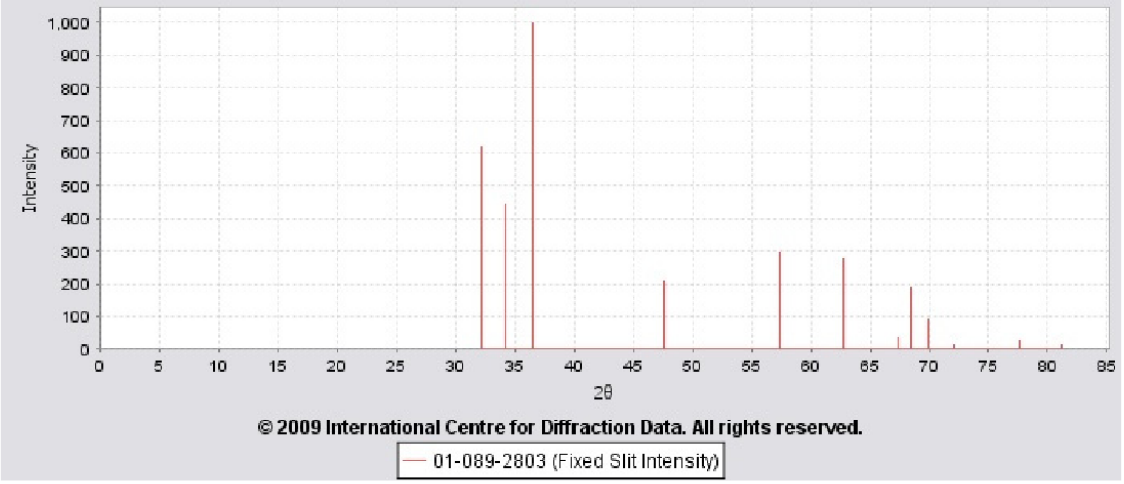

01-089-2803 (Fixed Slit Intensity)

2θ	d(Å)	Intensity	h	k	l
32.1731	2.7799	622	1	0	0
34.1952	2.62	445	0	0	2
36.5596	2.4558	999	1	0	1
47.6552	1.9067	210	1	0	2
57.361	1.605	298	1	1	0
62.7734	1.479	276	1	0	3
67.3055	1.39	38	2	0	0
68.5026	1.3686	189	1	1	2
69.9667	1.3435	89	2	0	1
72.0304	1.31	14	0	0	4
77.7046	1.2279	28	2	0	2
81.087	1.185	13	1	0	4

Appendix D

Cobalt oxide (III) PDF

PDF Card

PDF Number	00-042-1467		**Status**	Primary	**Quality Mark**		Star (S)
Pressure/Temperature	Ambient						
Chemical Formula	Co3 O4						
Weight %	Co73.42 O26.58						
Atomic %	Co42.86 O57.14						
Compound Name	Cobalt Oxide						
ANX							
Mineral Name							
Also Called							
Experimental	**Rad**	**λ**	**Filter**	**d-Spacing**	**Cutoff**	**Intensity**	**I/Ic**
	CuKá1	1.5406	Graph Mono	Diff.	15	Diffractometer	3.1
	Camera Diameter	**Reference**					
		Martin, K., McCarthy, G., North Dakota State University, Fargo, North Dakota, USA. ICDD Grant-in-Aid (1990).					
Physical	**SYS**	**Space Group**	**Aspect**				
	Cubic	Fd-3m (227)					
	Author's Cell	**a**	**b**	**c**	**α**	**β**	**γ**
		8.0837					
		Volume					
		528.24					
	Reference	Ibid.					
	Dcalc	**Dmeas**	**Dstruc**	**SS/FOM** F *21.0* =	**Melting Point**	**Z**	**R-factor**
	6.056			263 (0.003, 25.0)		8	
	Error						
Crystal	**Space Group**	**Z**	**Molecular Weight**				
	Fd-3m (227)	8	240.8				
	Crystal Cell	**a**	**b**	**c**	**α**	**β**	**γ**
		8.084	8.084	8.084	90	90	90
		Volume					
		528.24					
	Crystal Axial Ratio	**a/b**	**c/b**				
		a	**b**	**c**	**α**	**β**	**γ**
		5.716	5.716	5.716	60	60	60

	Reduced Cell	Volume 132.06
Optical	εα	nωβ / εγ / Sign / 2V
	Reference	
Structure	TF Type	
	Origin	
	Atomic Coordinates	Atom, Num, Wyckoff, Symmetry, x, y, z, SOF, ITF, AET
	SG Symmetry Operators	Seq, Operator
	Anisotropic Temperature Factors	Atom, Num, ATF11, ATF22, ATF33, ATF12, ATF13, ATF23
Miscellaneous	CAS Number	
	Pearson	cF56.00
	Pearson w/o H	
	Subfile Indicator	Common Phase, Corrosion, Inorganic, Metals & Alloys, Primary Pattern
	Prototype Structure	Al2 Mg O4
	LPF Prototype Structure	
	Mineral Classification	
	Zeolite Classification	
	Entry Date	02/28/1991
	Last Modification Date	01/24/2006
	Former PDF #	
	Cross-Reference PDF #'s	00-009-0418 (Deleted), 04-005-4386
Comments	Database Comments	
	User Comments	
	Shared Comments	

d-Spacings

λ =1.54056

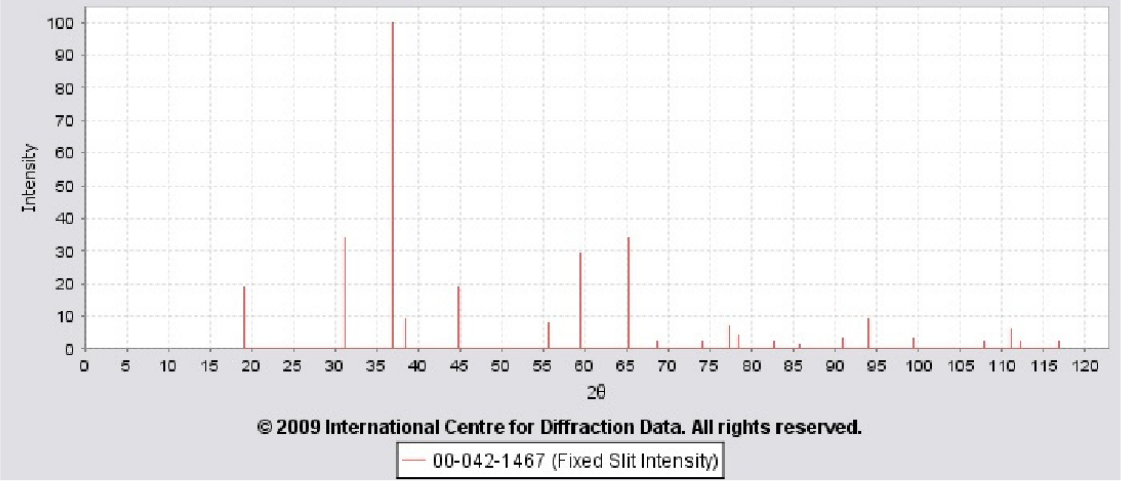

00-042-1467 (Fixed Slit Intensity)

2θ	d(Å)	Intensity	h	k	l
19.0001	4.667	19	1	1	1
31.2711	2.858	34	2	2	0
36.8517	2.437	100	3	1	1
38.5407	2.334	9	2	2	2
44.8084	2.021	19	4	0	0
55.6546	1.6501	8	4	2	2
59.3572	1.5557	29	5	1	1
65.2358	1.429	34	4	4	0
68.6282	1.3664	2	5	3	1
74.1168	1.2782	2	6	2	0
77.3382	1.2328	7	5	3	3
78.4031	1.2187	4	6	2	2
82.6248	1.1668	2	4	4	4
85.7591	1.132	1	7	1	1
90.9738	1.0802	3	6	4	2
94.0964	1.0524	9	7	3	1
99.3305	1.0105	3	8	0	0
107.9038	0.9527	2	6	6	0
111.2259	0.9334	6	7	5	1
112.3352	0.9273	2	6	6	2
116.9185	0.9038	2	8	4	0

Summary

In this report we present the growth process of the cobalt oxide system using reactive electron beam deposition. In that technique, a target of metallic cobalt is evaporated and its atoms are in-flight oxidized in an oxygen rich reactive atmosphere before reaching the surface of the substrate. With a trial and error procedure the deposition parameters have been optimized to obtain the correct stoichiometry and crystalline phase. The evaporation conditions to achieve the correct cobalt oxide salt rock structure, when evaporating over amorphous silicon nitride, are: 525 K of substrate temperature, $2.5{\cdot}10^{-4}$ mbar of oxygen partial pressure and 1 Å/s of evaporation rate. Once the parameters were optimized a set of ultra thin film ranging from samples of 1 nm of nominal thickness to 20nm thick and bulk samples were grown. With the aim to characterize the samples and study their microstructure and morphology, X-ray diffraction, transmission electron microscopy, electron diffraction, energy dispersive X-ray spectroscopy and quasi-adiabatic nanocalorimetry techniques are utilised. The final results show a size dependent effect of the antiferromagnetic transition. Its Néel temperature becomes depressed as the size of the grains forming the layer decreases.